# Protracted Kondo screening and kagome bands in the heavy-fermion metal $Ce_3Al$

Li Huang* and Haiyan Lu

*Science and Technology on Surface Physics and Chemistry Laboratory, P.O. Box 9-35, Jiangyou 621908, China*

(Received 26 April 2020; revised 12 October 2020; accepted 13 October 2020; published 26 October 2020)

$Ce_3Al$ is an archetypal heavy-fermion compound with multiple crystalline phases. Here, we try to investigate its electronic structures in the hexagonal phase ($\alpha$-$Ce_3Al$) and cubic phase ($\beta$-$Ce_3Al$) by means of a combination of density functional theory and single-site dynamical mean-field theory. We confirm that the $4f$ valence electrons in both phases are itinerant, accompanied by strong valence state fluctuations. Their $4f$ band structures are heavily renormalized by electronic correlations, resulting in large effective electron masses. The Kondo screening in both phases would be protracted over a wide range of temperature since the single-impurity Kondo temperature $T_K$ is much higher than the coherent Kondo temperature $T_K^*$. Especially, the crystal structure of $\alpha$-$Ce_3Al$ forms a layered kagome lattice. We observe conspicuous kagome-derived flat bands and Dirac cones (or gaps) in its quasiparticle band structure. Therefore, it is suggested that the hexagonal phase of $Ce_3Al$ is a promising candidate for a heavy-fermion kagome metal.

DOI: 10.1103/PhysRevB.102.155140

## I. INTRODUCTION

The discovery of fully gapped $d$-wave superconductivity in $CeCu_2Si_2$ has triggered a great deal of interest in heavy-fermion materials [1–5]. These materials are typically intermetallic compounds containing rare earths (Ce, Sm, and Yb) or actinides (U, Np, and Pu). They exhibit a variety of unusual properties that we still do not fully understand. For example, in comparison to normal metals, they have enormous values for the effective electron masses $m^*$, linear specific heat coefficients $\gamma$, and low-temperature magnetic susceptibilities $\chi$ [6]. Even more fascinating, the heavy-fermion materials may host a plethora of atypical phenomena and exotic quantum states, including quantum criticality, unconventional superconductivity, non-Fermi-liquid states, the topological Kondo insulator, and topological Kondo semimetals [7–12], just to name a few. Due to these tantalizing properties, the search for and characterization of heavy-fermion materials have become a rapid growing field in condensed-matter physics.

It is worth noting that quite a large portion of heavy-fermion materials are cerium-based intermetallic compounds [13]. They have attracted more attention than the other uranium-based and ytterbium-based heavy-fermion compounds [6]. For example, $CeCu_2Si_2$ is the first known heavy-fermion superconductor [1], as mentioned before. However, after 40 years, the exact symmetry of its superconducting gap has not been settled yet [14–16]. $CeCoIn_5$ is another heavy-fermion superconductor with a relatively high $T_c$ ($T_c > 2.3$ K). Besides unconventional superconductivity, it also exhibits spin-density-wave magnetic ordering [17], Fulde-Ferrell-Larkin-Ovchinnikov states [18], and antiferromagnetic quantum critical points [19–21], which can be easily modulated by external conditions, such as temperature, pressure, magnetic field, and chemical doping. Recently, it was used as a test bed to unveil the quasiparticle dynamics (collective hybridization between localized $4f$ moments and conduction electrons) at $T > T^*$, where $T^*$ marks the heavy-fermion coherence temperature [22]. The third example concerns cerium-based heavy-fermion topological semimetals, which provide a promising setting to study topological semimetals [23] driven by electronic correlations. For instance, $Ce_3Bi_4Pd_3$, a heavy-fermion system without centrosymmetry and magnetic order, was recently found to be a realization of the so-called Weyl-Kondo semimetal [7,24–26], which features strongly renormalized Weyl nodes in the bulk and hosts Fermi arcs on the surface.

Now let us concentrate on an "ancient" cerium-aluminum heavy-fermion system, $Ce_xAl_y$. It contains at least four stable intermetallic compounds, specifically, $CeAl_y$ ($y = 1, 2, 3$) and $Ce_3Al$. The ground states of both CeAl and $CeAl_2$ are antiferromagnetic with complicated ordering. Below 3.5 K, $CeAl_2$ enters an antiferromagnetic phase, in which the magnitudes and directions of the magnetic moments exhibit spatial periodicity. It is generally believed that this spin-density-wave-like antiferromagnetic ordering develops out of hybridization between localized $4f$ spins and conduction electrons (i.e., the Kondo effect) [27]. $CeAl_3$ is known to be the first discovered heavy-fermion metal with tremendous magnitude of the linear specific heat term [$\gamma = 1620$ mJ/(mole K$^2$)] [28]. Its ground state is also antiferromagnetic with $T_N = 1.2$ K [29]. As for $Ce_3Al$, at room temperature it crystallizes into a hexagonal $Ni_3Sn$-type structure [i.e., $\alpha$-$Ce_3Al$; see Figs. 1(a) and 1(b)]. Above 500 K, it transforms into a cubic $Cu_3Au$-type structure [i.e., $\beta$-$Ce_3Al$; see Fig. 1(c)]. Below 115 K, another structural phase transition occurs, and the monoclinic $\gamma$ phase appears. Antiferromagnetic ordering develops below 2.5 K [30]. Previous studies have revealed concrete fingerprints of heavy-fermion behaviors in the thermodynamic, magnetic, and transport properties of $Ce_3Al$ [31–33]. Strictly, $Ce_3Al$ is classified as a heavy-fermion system because of the large linear

*lihuang.dmft@gmail.com

 

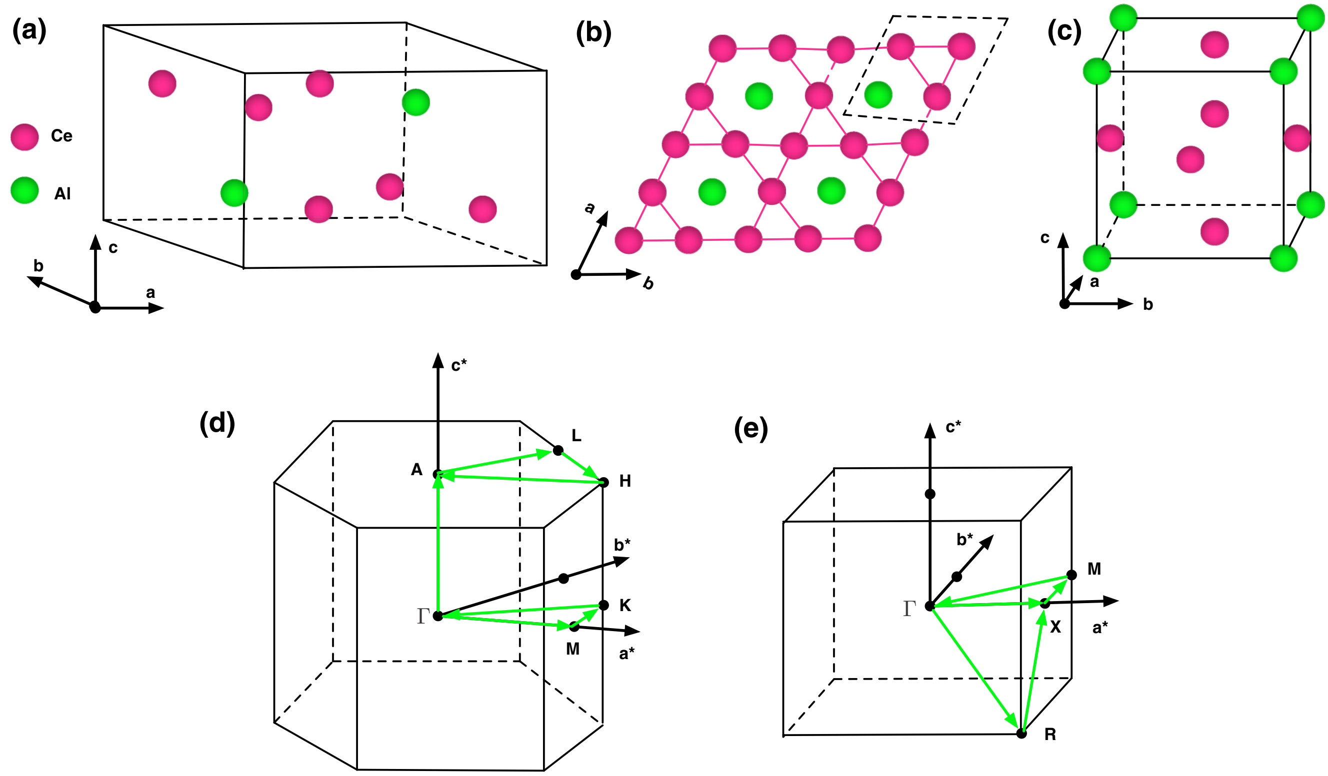


FIG. 1. (a) and (c) Crystal structures of $\alpha$- and $\beta$-$Ce_3Al$. Here, Ce and Al atoms are represented by red and green balls, respectively. (b) The kagome layer of $\alpha$-$Ce_3Al$ is illustrated. The dashed rhomboid indicates the unit cell. (d) and (e) Schematic pictures of Brillouin zones of $\alpha$- and $\beta$-$Ce_3Al$. Some selected high-symmetry directions are visualized by green arrows.

specific heat coefficient [$\gamma = 85$–$114$ mJ/(mole Ce K$^2$)] [34], but its $4f$ electrons are not as heavy as those in $CeAl_y$ [31,32].

Among the intermetallic compounds made by Ce and Al, $CeAl_2$ and $CeAl_3$ have been the most extensively studied in relation to their magnetic and heavy-fermion properties [27–29]. On the other hand, only a few works have been reported for $Ce_3Al$ [30–33]. Consequently, we know little about the detailed electronic structures of $Ce_3Al$. The variation of the $4f$ electronic states across the $\alpha$, $\beta$, and $\gamma$ phases remains unknown so far. Therefore, in the present work, we make a systematic study of the electronic structures of the high-symmetry phases of $Ce_3Al$ ($\alpha$-$Ce_3Al$ and $\beta$-$Ce_3Al$) by means of a state-of-the-art first-principles many-body approach. We try to calculate the quasiparticle band structures, total and partial densities of states, self-energy functions, and valence state histograms of both phases. The Kondo temperatures and effective $4f$ electron masses are also measured. Our results show that the $4f$ electrons in both phases are itinerant and fluctuating heavily among various electronic configurations, but they are not coherently screened by conduction electrons to form a heavy Fermi-liquid state [35] in the temperatures that we are interested in. In addition, it is suggested that $\alpha$-$Ce_3Al$ is a prototype of a kagome metal, which is characterized by the coexistence of dispersionless and linearly dispersive energy bands near the Fermi level [36].

The rest of this paper is organized as follows. First, the computational details are introduced in Sec. II. Then in Sec. III, the major results, including the momentum-resolved spectral functions, density of states, Kondo temperatures, self-energy functions, and valence state histograms of the two phases, are presented and analyzed. Section IV is devoted to discussing the kagome-derived flat bands and Dirac cones (or gaps) in the quasiparticle band structure of $\alpha$-$Ce_3Al$. Finally, Sec. V serves as a short summary.

## II. METHOD

In the present work, we employ the single-site dynamical mean-field theory in combination with the density functional theory (dubbed DFT + DMFT) [37,38] to study the electronic structures of $\alpha$- and $\beta$-$Ce_3Al$. Notice that this method has been successfully applied to explore the physical properties of many cerium-based heavy-fermion materials [39–44].

The DFT calculations were done by using the WIEN2K code, which implements a full-potential linearized augmented plane-wave formalism [45]. We adopted the experimental crystal structures [31,33]. The muffin-tin radii for Ce and Al atoms were 2.5 and 2.4 a.u., respectively. $R_{\mathrm{MT}} \times K_{\mathrm{MAX}} = 7.0$. The Perdew-Burke-Ernzerhof functional [46], i.e., the generalized gradient approximation, was adopted to express the exchange-correlation potential. The $k$ meshes for Brillouin zone integrations for the $\alpha$- and $\beta$-$Ce_3Al$ phases were $15 \times 15 \times 16$ and $15 \times 15 \times 15$, respectively. The spin-orbit coupling was considered in all calculations explicitly.

Since the electronic correlations among Ce's $4f$ valence electrons are crucial, we have to take them into account. We utilized the DMFT method to treat the correlated nature of $4f$ electrons [37]. We used the EDMFT code developed by Haule *et al.* [43]. The system temperatures for $\alpha$- and $\beta$-$Ce_3Al$ were

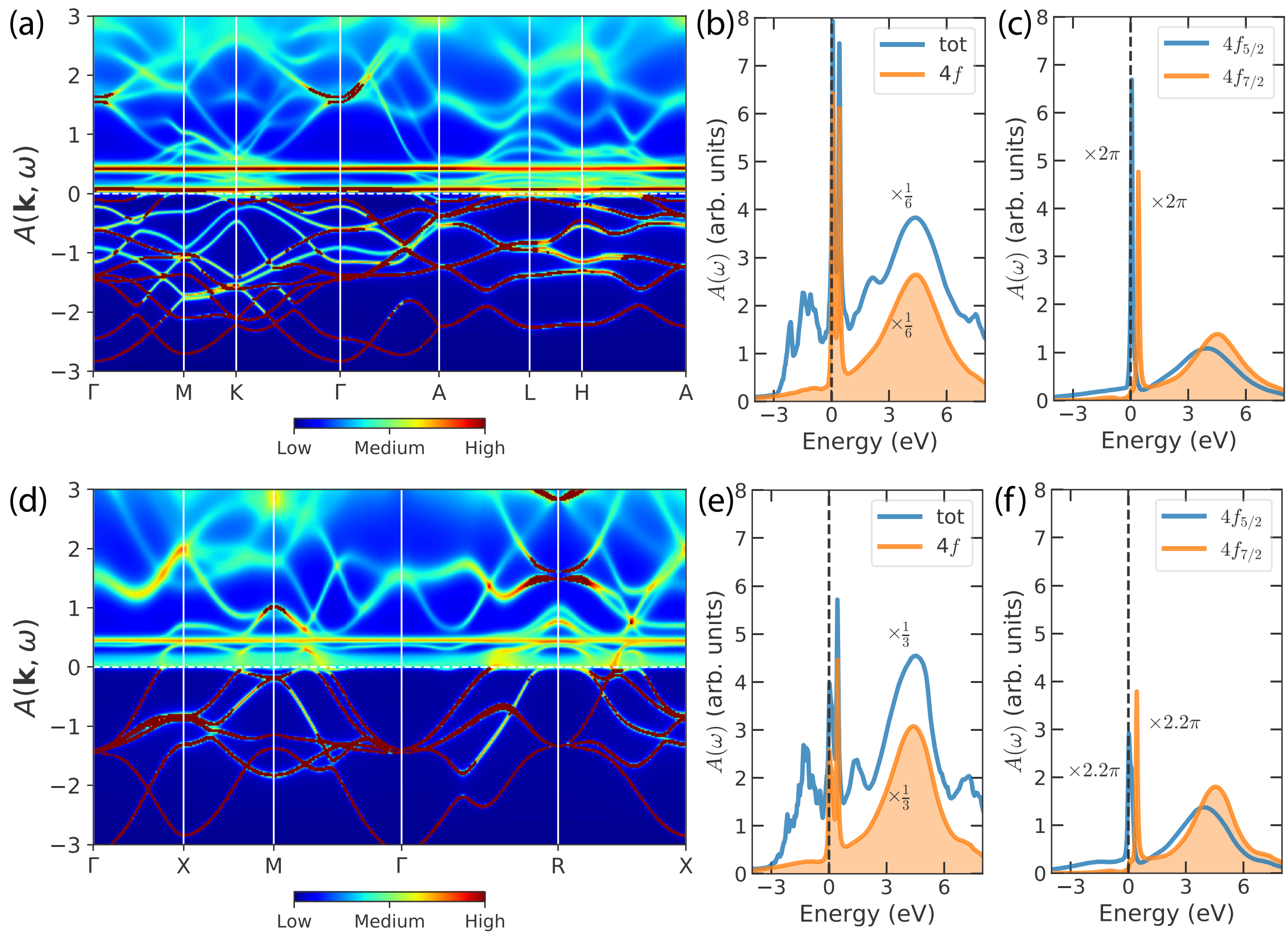


FIG. 2. Quasiparticle band structures of $Ce_3Al$ obtained via DFT + DMFT calculations. The results for the $\alpha$ and $\beta$ phases of $Ce_3Al$ are plotted in the top and bottom panels, respectively. (a) and (d) Momentum-resolved spectral functions $A(\mathbf{k}, \omega)$. (b) and (e) Total and $4f$ partial densities of states [i.e., $A(\omega)$ and $A_{4f}(\omega)$]. (c) and (f) $j$-resolved $4f$ partial density of states [i.e., $A_{4f_{5/2}}(\omega)$ and $A_{4f_{7/2}}(\omega)$]. Here, the horizontal and vertical dashed lines denote the Fermi level. The data for $A(\omega)$, $A_{4f}(\omega)$, $A_{4f_{5/2}}(\omega)$, and $A_{4f_{7/2}}(\omega)$ are rescaled for a better view.

set to be $T \approx 230$ K and $T \approx 580$ K, respectively. A large energy window (from $-10$ eV to $+10$ eV with respect to the Fermi level) was used to construct the DMFT projectors and local orbitals. The Coulomb repulsion interaction parameter $U$ and Hund's exchange interaction parameter $J_{\mathrm{H}}$ for Ce's $4f$ electrons were 6.0 and 0.7 eV, respectively [40–44]. The double-counting term for the self-energy functions was subtracted via the exact scheme [47]. In order to solve the auxiliary quantum impurity problems for the $4f$ electrons, a hybridization expansion continuous-time quantum Monte Carlo impurity solver (dubbed CT-HYB) [48–50] was used. For each quantum impurity solver run, the number of Monte Carlo steps was up to 200 million per CPU process. We performed charge fully self-consistent DFT + DMFT calculations. In order to obtain good convergence, the maximum number of DFT + DMFT iterations was set to 100.

## III. RESULTS

*Quasiparticle band structures.* The momentum-resolved spectral functions (or, equivalently, quasiparticle band structures) $A(\mathbf{k}, \omega)$ along some selected high-symmetry directions for the $\alpha$ and $\beta$ phases of $Ce_3Al$ are visualized in Figs. 2(a) and 2(d), respectively. The spectra of the two phases share some common characteristics. First, the spectra below the Fermi level look quite coherent and have large dispersions, which are attributed to the contributions of conduction electrons (see Fig. 8 as well). Second, the incoherent $4f$ bands dominate above the Fermi level, resulting in blur and diffused spectra. Third, we observe remarkable stripelike features near the Fermi level. One stripe pins exactly at the Fermi level (their positions are 0.06 eV for $\alpha$-$Ce_3Al$ and 0.09 eV for $\beta$-$Ce_3Al$), while the other is a few hundred meV above the Fermi level (their positions are 0.41 eV for $\alpha$-$Ce_3Al$ and 0.44 eV for $\beta$-$Ce_3Al$). These stripes are related to the spin-orbit splitting $4f_{5/2}$ and $4f_{7/2}$ bands, which have been seen in Ce metal [41] and some other cerium-based heavy-fermion compounds, such as $CeTIn_5$ [40,43], $CeIn_3$ [44], $CeB_6$ [51], and $CeM_2Si_2$ [42]. The low-lying $4f_{5/2}$ bands are extremely flat and intense, leading to sharp peaks at the Fermi level in the density of states. They signal the itinerant behaviors of the $4f$ electrons in $\alpha$- and $\beta$-$Ce_3Al$.

Figures 2(b) and 2(e) depict the total density of states $A(\omega)$ and $4f$ partial density of states $A_{4f}(\omega)$. $A_{4f}(\omega)$ shows

TABLE I. Important model parameters for the electronic structures of $\alpha$-$Ce_3Al$ and $\beta$-$Ce_3Al$. They include the width of the conduction band below the Fermi level $W$, the averaged $4f$ electron level $\epsilon_f$, the imaginary part of the hybridization function at the Fermi level $\mathrm{Im}\Delta(E_F)$, the density of states of conduction electrons at the Fermi level $\rho_c(E_F)$, the single-impurity Kondo temperature $T_K$, the coherent Kondo temperature $T_K^*$, the quasiparticle weights ($Z_{5/2}$ and $Z_{7/2}$), the renormalized electron masses ($m^*_{5/2}$ and $m^*_{7/2}$), and the probabilities of the $4f^0$, $4f^1$, and $4f^2$ configurations ($p_0$, $p_1$, and $p_2$). See the text for more details.

| Case | $W$[a,g] (eV) | $\epsilon_f$[b,g] (eV) | $\mathrm{Im}\Delta(E_F)$[c,g] (eV) | $\rho_c(E_F)$[d,g] ($\mathrm{eV}^{-1}$) | $T_K$[e] (K) | $T_K^*$ (K) | $Z_{5/2}$ | $Z_{7/2}$ | $m^*_{5/2}$[f] | $m^*_{7/2}$[f] | $p_0$ (%) | $p_1$ (%) | $p_2$ (%) |
|---|---|---|---|---|---|---|---|---|---|---|---|---|---|
| $\alpha$-$Ce_3Al$ | 7.05 | −1.60 | −0.147 | 8.37 | 684 | 56 | 0.17 | 0.41 | $5.88m_e$ | $2.45m_e$ | 8.56 | 85.36 | 6.01 |
| $\beta$-$Ce_3Al$ | 6.60 | −1.46 | −0.149 | 4.23 | 885 | 47 | 0.13 | 0.27 | $7.75m_e$ | $2.56m_e$ | 7.21 | 87.78 | 4.96 |

[a]We used the criterion $\rho_c(-lb) < 0.02\ \mathrm{eV}^{-1}$ to determine the left boundary ($lb$). Then according to the definition of $W$ ($W$ is the width of occupied conduction bands, instead of the full width of the conduction bands), $W = lb$.
[b]$\epsilon_f = [\epsilon_f(j = 5/2) + \epsilon_f(j = 7/2)]/2$.
[c]Only for the $4f_{5/2}$ states. See Fig. 7.
[d]$\rho_c(\omega) = A(\omega) - A_{4f}(\omega)$. See Fig. 8.
[e]Here, the single-impurity Kondo temperature $T_K$ was calculated using Eq. (1). In Ref. [54], a different formula for $T_K$ is suggested, which relies on only $Z$ and $\mathrm{Im}\Delta(E_F)$ [i.e., $T_K = -\pi Z \mathrm{Im}\Delta(E_F)/4$]. We also adopted this equation to evaluate $T_K$. The calculated results are approximately 230 and 180 K for $\alpha$- and $\beta$-$Ce_3Al$, respectively. Although they are much smaller than the present values, the major conclusions of this paper will not be modified.
[f]Here, $m_e$ denotes the mass of the noninteracting electron. The renormalized electron masses were calculated using Eq. (3). Note that they can be evaluated via the Matsubara self-energy functions directly: $m^*/m_e \approx 1.0 - \mathrm{Im}\Sigma(i\omega_0)/\omega_0$, where $\omega_0$ is the first Matsubara frequency point. Based on this equation, we obtained $m^*_{5/2} \approx 7.15m_e$ and $m^*_{7/2} \approx 3.17m_e$ for $\alpha$-$Ce_3Al$ and $m^*_{5/2} \approx 7.56m_e$ and $m^*_{7/2} \approx 3.01m_e$ for $\beta$-$Ce_3Al$. These results are roughly consistent with the present values.
[g]Note that $W$, $\epsilon_f$, $\mathrm{Im}\Delta(\omega)$, and $\rho_c(\omega)$ are calculated at the DFT + DMFT level.

a prominent three-peak structure, which is typical in strongly correlated metals [38]. The Abrikosov-Suhl-like quasiparticle peak (or Kondo resonance peak) is well developed at the Fermi level, similar to $\alpha$-Ce [41]. Due to the spin-orbit coupling effect, it is split into two subpeaks, which are counterparts of the stripelike structures seen in $A(\mathbf{k}, \omega)$. In addition, there is a broad and smooth "hump" between 2 and 8 eV. It is mainly assigned to the upper Hubbard bands of cerium's $4f$ orbitals. On the other hand, the lower Hubbard bands (residing from −3 to −0.5 eV) exhibit small spectral weights, which are consistent with the fact that most of cerium's $4f$ orbitals are unoccupied. In Figs. 2(c) and 2(f), we further show the $j$-resolved $4f$ partial density of states. We find that the energy separation between the $4f_{5/2}$ and $4f_{7/2}$ peaks is about 350 meV, which is somewhat larger than those in the other cerium-based heavy-fermion compounds [42–44]. Here, we introduce a new variable, $R$. It is the ratio of the heights of the two spin-orbit split peaks, i.e., $R \equiv h(4f_{5/2})/h(4f_{7/2})$. We obtain $R > 1.0$ for $\alpha$-$Ce_3Al$, while $R < 1.0$ for $\beta$-$Ce_3Al$. This difference can easily be explained by the temperature effect. When the temperature is increased, the $4f$ electrons should become more and more incoherent [39,40]. Thus, the low-lying $4f_{5/2}$ bands are suppressed, and so is $R$.

*Kondo screening.* The physical properties of heavy-fermion materials are controlled by two essential factors [6]. One is the Coulomb repulsion interaction among the localized $f$ electrons; another one is the hybridization (coupling) between localized $f$ electrons (localized $f$ moments) and conduction electrons. In the weak-hybridization limit, the Ruderman-Kittel-Kasuya-Yosida interaction dominates, which drives the localized $f$ electrons to yield magnetic ordering states. On the other hand, when the hybridization is strong, the Kondo mechanism begins to work. The localized moments of $f$ electrons are screened by conduction electrons, and a heavy Fermi-liquid state appears at low temperature. Traditionally, the Kondo temperature is defined to mark the energy scale of screening of a localized $f$ electron. We can use the following equation to make a rough estimation of the single-impurity Kondo temperature $T_K$ [52]:

$$T_K = \sqrt{W|\mathrm{Im}\Delta(E_F)|}\exp\left(-\frac{\pi|\epsilon_f|}{2N_f|\mathrm{Im}\Delta(E_F)|}\right). \tag{1}$$

Here, $W$ is the width of occupied conduction bands, $\mathrm{Im}\Delta(E_F)$ is the imaginary part of the hybridization function at the Fermi level, $\epsilon_f$ is the averaged impurity level for $4f_{5/2}$ and $4f_{7/2}$ states, and $N_f$ is the band degeneracy of $f$ electrons. Since the Kondo resonance peak in the Fermi level is mainly associated with the sixfold $4f_{5/2}$ states, $N_f = 6$ in Eq. (1). We can further evaluate the coherent Kondo temperature (or protracted Kondo screening temperature) $T_K^*$, which indicates the temperature that all localized $f$ electrons are screened by conduction electrons. Note that $T_K^*$ is related to $T_K$ via the following formula [35,53]:

$$T_K^* = \frac{\rho_c(E_F)}{N_f}T_K^2, \tag{2}$$

where $\rho_c(E_F)$ denotes the density of states of conduction electrons at the Fermi level. We tried to calculate $T_K$ and $T_K^*$ for $\alpha$- and $\beta$-$Ce_3Al$ with Eqs. (1) and (2). The calculated results, together with the necessary parameters, are summarized in Table I. Nozières's exhaustion theory [35] argues that only those conduction electrons within the Kondo energy scale around the Fermi level $E_F$ can contribute to the screening process. As a consequence, the coherent Kondo temperature $T_K^*$ could be much lower than the single-impurity Kondo temperature $T_K$ in heavy-fermion materials with low carrier density [55]. Our results clearly reveal that $T_K \gg T_K^*$, which

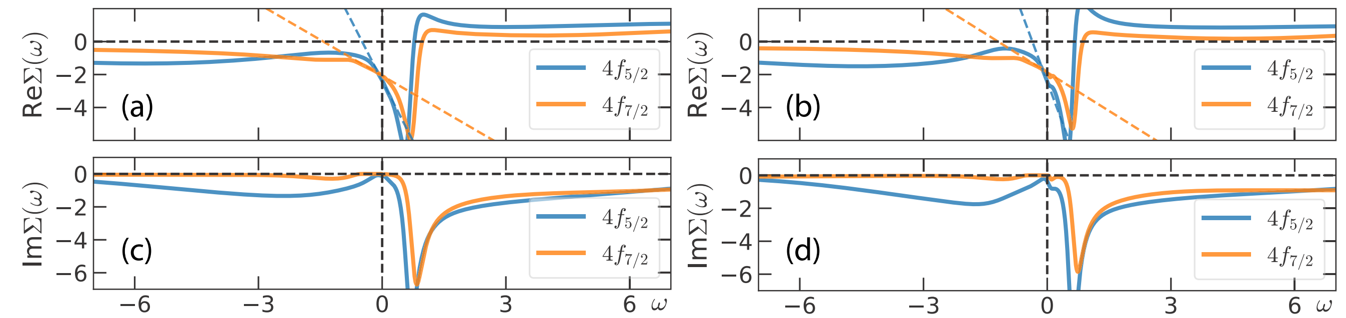


FIG. 3. Real and imaginary parts of self-energy functions of Ce $4f$ electrons at the real axis for (a) and (c) $\alpha$-$Ce_3Al$ and (b) and (d) $\beta$-$Ce_3Al$. In (a) and (b), the blue and yellow dashed lines are linear fits for the low-frequency quasilinear regimes of the self-energy functions. See the text for more explanations.

suggests that both phases are in the protracted Kondo screening states over a wide range of temperature ($T_K > T > T_K^*$) [53]. The low-temperature resistivity of $\alpha$-$Ce_3Al$ exhibits two characteristic maximums around 100 and 3 K and a minimum around 20 K. The high-temperature anomaly may be due to the $\alpha$-$\gamma$ phase transition, and the low-temperature anomaly may originate from the occurrence of antiferromagnetic order. As for the resistance minimum, previous studies suggested that it marks the onset of the Kondo screening (Kondo minimum) [30,31,34]. Instead, we believe that it denotes a phase transition from the protracted Kondo screening state to the coherent Kondo screening state.

*Self-energy functions.* Next, let us examine the heavy-fermion states in $Ce_3Al$. First, we have to perform analytical continuation for the self-energy functions at the Matsubara axis $\Sigma(i\omega_n)$ via the maximum-entropy method [56]. The obtained self-energy functions at real axis $\Sigma(\omega)$ are shown in Fig. 3. We detect that the orbital differentiation in the self-energy functions is considerable. For the imaginary parts of self-energy functions $\mathrm{Im}\Sigma(\omega)$, sizable gaps occur at $\omega = 0$ for the $4f_{7/2}$ states. However, $|\mathrm{Im}\Sigma(\omega)|$ for the $4f_{5/2}$ states are finite. They imply the existence of low-energy electron scattering. For the real parts of self-energy functions $\mathrm{Re}\Sigma(\omega)$, we observe quasilinear behaviors in the vicinity of the Fermi level. Therefore, we can utilize the following equation to evaluate the quasiparticle weights $Z$ and effective electron masses $m^*$ [38]:

$$Z^{-1} = \frac{m^*}{m_e} = 1 - \frac{\partial \mathrm{Re}\Sigma(\omega)}{\partial \omega}\bigg|_{\omega=0}. \qquad (3)$$

The calculated results are tabulated in Table I. Just as expected, the $4f$ electron correlations are orbital dependent. The low-lying $4f_{5/2}$ states are more correlated than the high-lying $4f_{7/2}$ states ($Z_{5/2} < Z_{7/2}$), so the $4f$ electrons in the $j = 5/2$ states suffer more renormalization and become heavier. It is not surprising that the $4f$ electrons in $Ce_3Al$ are much lighter than those in the other Ce-Al intermetallic heavy-fermion compounds. After all $\gamma_{Ce_3Al}/\gamma_{CeAl_3} \approx 0.2$ [28,34].

*Valence state histograms.* Valence fluctuation and mixed-valence behavior are general features in correlated $f$-electron systems [41,43]. Especially, when the $f$ electrons reside on the itinerant side (strong hybridization limit), these effects will become more prominent [41]. In this work, we tried to calculate the valence state histograms (i.e., atomic eigenstates probabilities) of $Ce_3Al$ to quantify its valence fluctuations [48]. See Fig. 4 for the histograms. Here, we use three good quantum numbers to label these atomic eigenstates, i.e., total occupancy $N$, total angular momentum $J$, and $\gamma$, which stands for the rest of the atomic quantum numbers, such as $J_z$. We have the following findings. At first glance, the distributions of valence state histograms of $\alpha$- and $\beta$-$Ce_3Al$ are quite similar. They are diverse. Accordingly, the valence state fluctuations in both phases are intense. Second, the probability of the $4f^1$ configuration is undoubtedly overwhelming. But the contributions from the other configurations, such as $4f^0$ and $4f^2$, are also crucial (see Table I). The contributions from $4f^3$ and those with more $4f$ occupancies are negligible. With this information, we can easily calculate the expected $4f$ occupancy $\langle N\rangle$ and expected total angular momentum $\langle J\rangle$. For $\alpha$-$Ce_3Al$, $\langle N\rangle \approx 0.976$, and $\langle J\rangle \approx 2.47$. However, for $\beta$-$Ce_3Al$, $\langle N\rangle \approx 0.978$, and $\langle J\rangle \approx 2.46$. These data are quite close. Third, the ground states of both phases are $|N = 1, J = 2.5, \gamma = 0\rangle$, which is the same as for Ce and most of the cerium-based heavy-fermion systems [42,44,51]. Their probabilities are 75.7% for $\alpha$-$Ce_3Al$ and 80.9% for $\beta$-$Ce_3Al$.

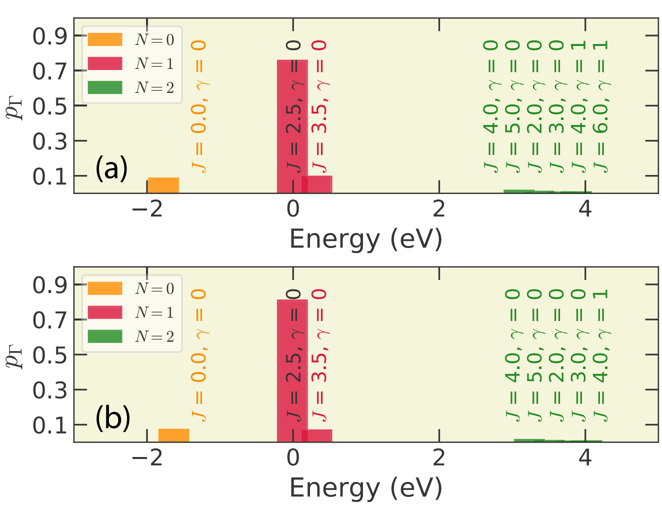


FIG. 4. Valence state histograms of Ce's $4f$ electrons. The data for the $4f^3$ ($N = 3$) configurations are too trivial to be seen. (a) $\alpha$-$Ce_3Al$. (b) $\beta$-$Ce_3Al$.

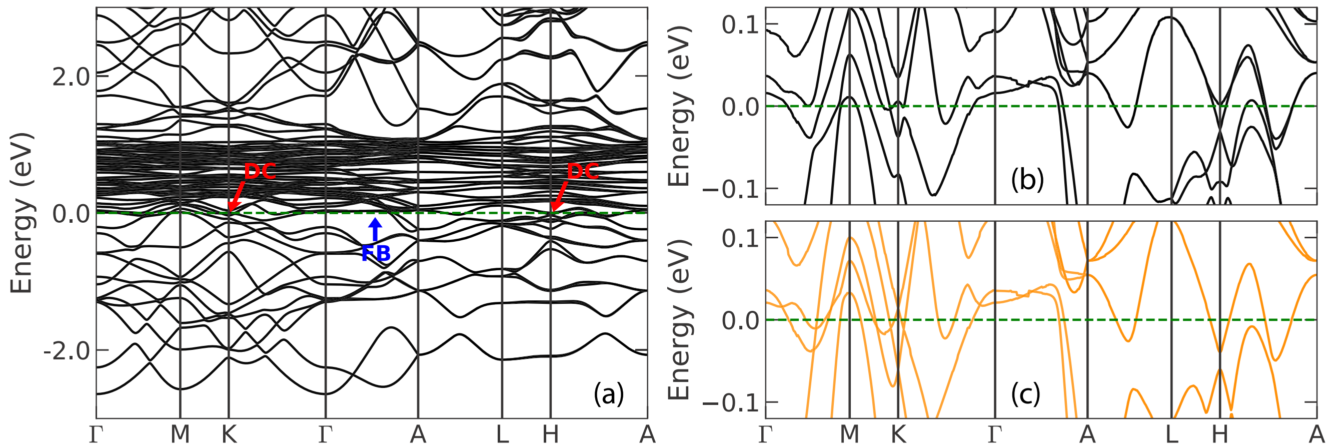


FIG. 5. (a) and (b) Electronic band structures of $\alpha$-$Ce_3Al$ obtained via DFT + SOC calculations. (c) Electronic band structure of $\alpha$-$Ce_3Al$ obtained via DFT calculations. Here, DC is Dirac cone, and FB is an abbreviation of flat band. The horizontal dashed line denotes the Fermi level. Note that the Dirac cones or gaps at the $K$ and $H$ points should be tuned by spin-orbit coupling.

Finally, note that the data presented here are quite analogous to those for $\alpha$-Ce ($\langle N\rangle \approx 0.98$, $\langle J\rangle \approx 2.45$, and the probability of $|N = 1, J = 2.5, \gamma = 0\rangle$ is approximately 68.31%) [41,48], in which the $4f$ electrons are known to be itinerant and strongly hybridize with conduction electrons. So, to some extent, the $4f$ electronic structures of $Ce_3Al$ and $\alpha$-Ce are similar.

## IV. DISCUSSION

Very recently, the concept of kagome lattice and kagome metals has attracted quite a lot of attention [36]. The kagome lattice or kagome pattern is a two-dimensional network of trihexagonal tiling. If conductive materials are made to resemble some kind of kagome lattice at the atomic scale, they are the so-called kagome metals. From the viewpoint of band topology, the signature of kagome metals is the coexistence of kagome-derived dispersionless flat bands and band crossings between two linearly dispersive bands (i.e., Dirac cones) [57–59]. When the spin-orbit coupling (SOC) is considerable, Dirac gaps are opened, and massive Dirac fermions emerge [60]. Thus, the kagome metals provide ideal platforms to study the interplay between topology and electronic correlation. Up to now, most of the available kagome metals are correlated $d$-electron systems, containing Fe, Co, and Mn transition metal elements [57–70]. To our knowledge, the $f$-electron kagome metals are still absent. It would be interesting to search for kagome metals in rare-earth and actinide compounds, especially in the cerium-based heavy-fermion materials.

Notice that the crystal structure of $\alpha$-$Ce_3Al$ can be viewed as a sequence stacking of a kagome layer along the $c$ axis [see Figs. 1(a) and 1(b)]. Its kagome layer consists of Ce atoms, and the centers of the hexagons are populated by Al atoms. Compared to the other kagome metals [58,60,69,71], $\alpha$-$Ce_3Al$ has no spacing layer. Nevertheless, a question is naturally

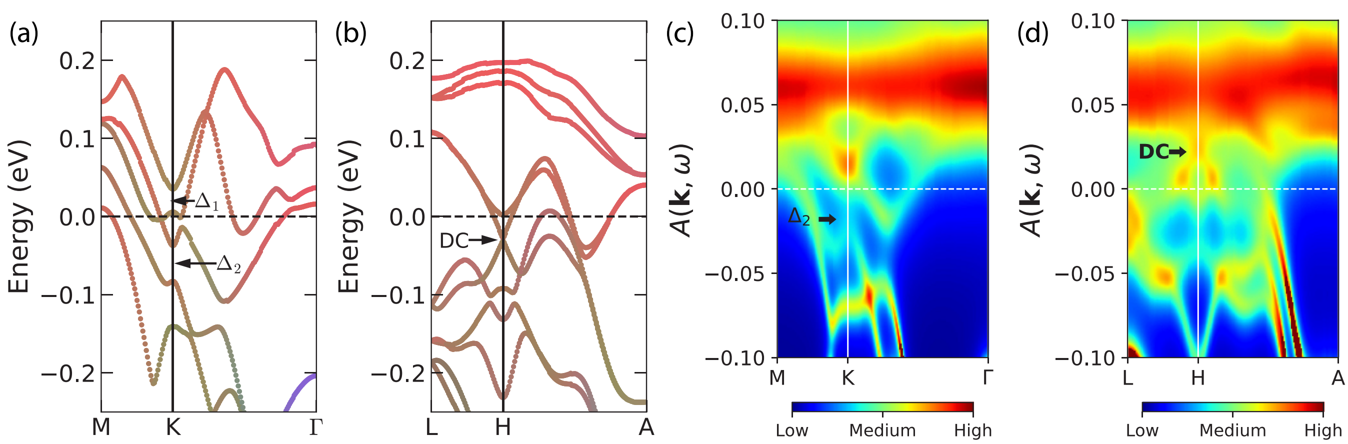


FIG. 6. (a) and (b) DFT + SOC band structures for $\alpha$-$Ce_3Al$ in some selected high-symmetry directions. Here, colors are used to distinguish different orbital characteristics (red: Ce $4f$; green: Ce $5d$; blue: Al $3p$), $\Delta_1 \sim \Delta_2$ mark the Dirac band gaps opened by SOC, DC means the Dirac cone. (c) and (d) Quasiparticle band structures for $\alpha$-$Ce_3Al$ using the DFT + DMFT method in the same high-symmetry directions as in (a) and (b). Here, $\Delta_2$ and DC mean the renormalized Dirac gap and Dirac cone, respectively.

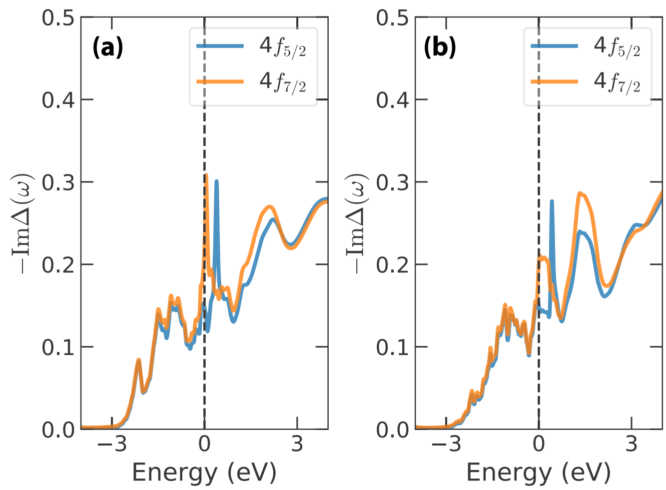


FIG. 7. Imaginary parts of hybridization functions $-\mathrm{Im}\Delta(\omega)$ obtained by the DFT + DMFT method for (a) $\alpha$-$Ce_3Al$ and (b) $\beta$-$Ce_3Al$. The vertical dashed lines denote the Fermi level. From this figure, we can determine $\mathrm{Im}\Delta(E_F)$.

raised. Is $\alpha$-$Ce_3Al$ a candidate for a heavy-fermion kagome metal? In other words, can we observe kagome-derived flat bands and Dirac cones simultaneously in the electronic structure of $\alpha$-$Ce_3Al$? In order to answer these questions, we made a further analysis of the DFT + SOC and DFT + DMFT band structures of $\alpha$-$Ce_3Al$.

We at first carried out DFT and DFT + SOC calculations for $\alpha$-$Ce_3Al$ to exclude the effect of electronic correlation. Figure 5 shows the calculated band structure. We see that the extremely flat bands, which are largely attributed to the $4f$ orbitals of Ce atoms, spread over the whole Brillouin zone. At the high-symmetry $K$ and $H$ points, there are some crossing points made by linearly dispersive bands. In Fig. 5(a), some representative flat bands and Dirac cones (or Dirac gaps) near the Fermi level are annotated by arrows. Enlarged views of these bands are illustrated in Figs. 5(b) and 5(c), and the corresponding fat bands are plotted in Figs. 6(a) and 6(b). The Dirac cones at the $K$ point have $4f$ character. They are opened by the spin-orbit coupling to yield two Dirac gaps, $\Delta_1$ and $\Delta_2$. Interestingly, the spin-orbit coupling leads to a converse consequence at the $H$ point. It closes a Dirac gap and recovers a Dirac cone [labeled DC in Fig. 6(b)]. Anyway, all these characteristics suggest that $\alpha$-$Ce_3Al$ is a candidate for a kagome metal with heavy fermions. These dispersionless flat bands and Dirac cones (or Dirac gaps) are, indeed, kagome-derived features, instead of being a consequence of strong $4f$ electronic correlation or $c$-$f$ hybridization effect.

Next, we wonder whether these kagome-related features will be destroyed by strong electronic correlation. In Figs. 6(c) and 6(d), the corresponding quasiparticle band structures obtained by DFT + DMFT calculations are shown. First of all, the kagome-derived flat bands are strongly renormalized. The bandwidth is greatly reduced, and the central energy level is shifted upward. Second, the Dirac gap $\Delta_1$ is destroyed. Although the Dirac gap $\Delta_2$ still survives, it is obviously shifted toward the Fermi level. Third, the Dirac cone at the $H$ point (DC) is pushed onto the Fermi level and touches the flat bands. The nearby band structures are quite incoherent. As a whole, the influence of $4f$ electronic correlation on the kagome-derived bands cannot be ignored in this case. Our results imply that there should be a competition between the kagome mechanism and the electronic correlation.

## V. SUMMARY

In summary, we performed charge fully self-consistent DFT + DMFT calculations to study the detailed electronic structures of $\alpha$-$Ce_3Al$ and $\beta$-$Ce_3Al$. Their quasiparticle band structures, density of states, self-energy functions, and valence state histograms were determined. Both phases are typical

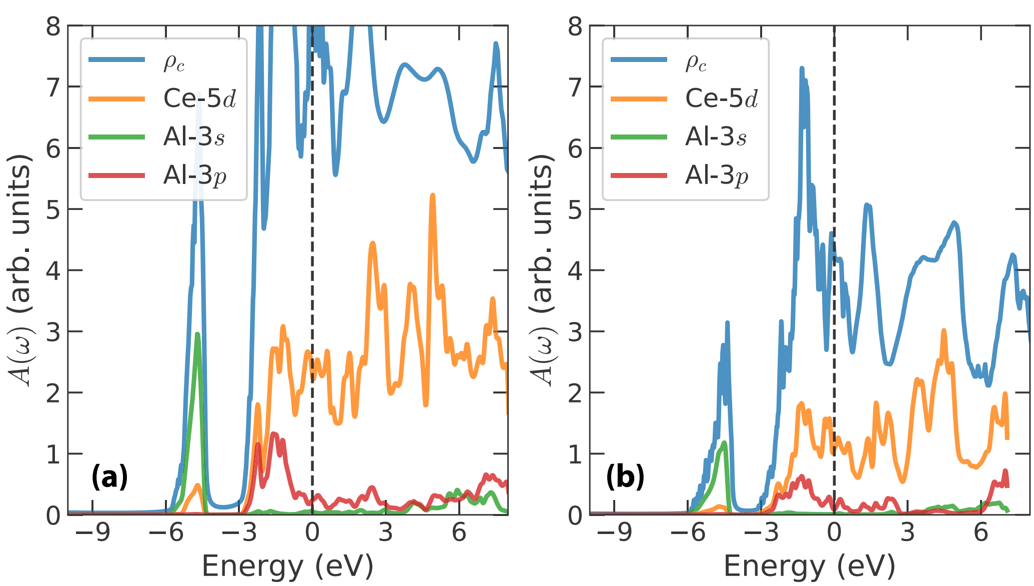


FIG. 8. Density of states for conduction bands $\rho_c$ and partial density of states for Ce $5d$, Al $3s$, and Al $3p$ orbitals obtained by the DFT + DMFT method for (a) $\alpha$-$Ce_3Al$ and (b) $\beta$-$Ce_3Al$. The vertical dashed lines denote the Fermi level. From this figure, we can determine $W$ and $\rho_c(E_F)$.

heavy-fermion metals. Their $4f$ electrons tend to be itinerant and strongly hybridize with the conduction electrons. The $4f$ valence state fluctuations are comparable to those in $\alpha$-Ce. We estimated the single-impurity Kondo temperature $T_K$ and the coherent Kondo temperature $T_K^*$. We figured out that $T_K \gg T_K^*$, which agrees with the prediction of Nozières's exhaustion theory and suggests that both phases would retain the protracted Kondo screening state over a wide range of temperature. In addition, clear signatures of a kagome metal, including dispersionless flat bands and linearly dispersive bands, were identified in the band structure of $\alpha$-$Ce_3Al$. Thus, it is concluded that the $\alpha$ phase of $Ce_3Al$ is a candidate for a heavy-fermion kagome metal. This material should provide a fertile playground to study the entanglement of topology, Kondo screening, and heavy-fermion behavior. Further experiments and theoretical studies to validate our predictions are highly desired.

## ACKNOWLEDGMENTS

This work was supported by the Natural Science Foundation of China (Grants No. 11874329, No. 11934020, and No. 11704347) and the Science Challenge Project of China (Grant No. TZ2016004).

## APPENDIX: HYBRIDIZATION FUNCTIONS AND DENSITY OF STATES FOR CONDUCTION BANDS

In Figs. 7 and 8, the imaginary parts of hybridization functions $|\mathrm{Im}\Delta(\omega)|$ and density of states of conduction bands $\rho_c$ and partial density of states for Ce $5d$, Al $3s$, and Al $3p$ orbitals are shown, respectively. From these figures, we can easily extract the necessary parameters, with which the single-impurity Kondo temperature $T_K$ and coherent Kondo temperature $T_K^*$ (see Table I) are estimated using Eqs. (2) and (3).

[1] F. Steglich, J. Aarts, C. D. Bredl, W. Lieke, D. Meschede, W. Franz, and H. Schäfer, Phys. Rev. Lett. **43**, 1892 (1979).
[2] O. Stockert, J. Arndt, E. Faulhaber, C. Geibel, H. S. Jeevan, S. Kirchner, M. Loewenhaupt, K. Schmalzl, W. Schmidt, Q. Si, and F. Steglich, Nat. Phys. **7**, 119 (2011).
[3] G. Pang, M. Smidman, J. Zhang, L. Jiao, Z. Weng, E. M. Nica, Y. Chen, W. Jiang, Y. Zhang, W. Xie, H. S. Jeevan, H. Lee, P. Gegenwart, F. Steglich, Q. Si, and H. Yuan, Proc. Natl. Acad. Sci. USA **115**, 5343 (2018).
[4] T. Yamashita, T. Takenaka, Y. Tokiwa, J. A. Wilcox, Y. Mizukami, D. Terazawa, Y. Kasahara, S. Kittaka, T. Sakakibara, M. Konczykowski, S. Seiro, H. S. Jeevan, C. Geibel, C. Putzke, T. Onishi, H. Ikeda, A. Carrington, T. Shibauchi, and Y. Matsuda, Sci. Adv. **3**, e1601667 (2017).
[5] H. Q. Yuan, F. M. Grosche, M. Deppe, C. Geibel, G. Sparn, and F. Steglich, Science **302**, 2104 (2003).
[6] G. R. Stewart, Rev. Mod. Phys. **56**, 755 (1984).
[7] H.-H. Lai, S. E. Grefe, S. Paschen, and Q. Si, Proc. Natl. Acad. Sci. **115**, 93 (2018).
[8] M. Dzero, J. Xia, V. Galitski, and P. Coleman, Annu. Rev. Condens. Matter Phys. **7**, 249 (2016).
[9] G. R. Stewart, Rev. Mod. Phys. **73**, 797 (2001).
[10] M. Dzero, K. Sun, V. Galitski, and P. Coleman, Phys. Rev. Lett. **104**, 106408 (2010).
[11] E. Schuberth, M. Tippmann, L. Steinke, S. Lausberg, A. Steppke, M. Brando, C. Krellner, C. Geibel, R. Yu, Q. Si, and F. Steglich, Science **351**, 485 (2016).
[12] P. Gegenwart, Q. Si, and F. Steglich, Nat. Phys. **4**, 186 (2008).
[13] Z. F. Weng, M. Smidman, L. Jiao, X. Lu, and H. Q. Yuan, Rep. Prog. Phys. **79**, 094503 (2016).
[14] S. Kitagawa, G. Nakamine, K. Ishida, H. S. Jeevan, C. Geibel, and F. Steglich, Phys. Rev. Lett. **121**, 157004 (2018).
[15] Y. Li, M. Liu, Z. Fu, X. Chen, F. Yang, and Y.-f. Yang, Phys. Rev. Lett. **120**, 217001 (2018).
[16] S. Kittaka, Y. Aoki, Y. Shimura, T. Sakakibara, S. Seiro, C. Geibel, F. Steglich, H. Ikeda, and K. Machida, Phys. Rev. Lett. **112**, 067002 (2014).
[17] D. Y. Kim, S.-Z. Lin, F. Weickert, M. Kenzelmann, E. D. Bauer, F. Ronning, J. D. Thompson, and R. Movshovich, Phys. Rev. X **6**, 041059 (2016).
[18] C. F. Miclea, M. Nicklas, D. Parker, K. Maki, J. L. Sarrao, J. D. Thompson, G. Sparn, and F. Steglich, Phys. Rev. Lett. **96**, 117001 (2006).
[19] J. Paglione, M. A. Tanatar, D. G. Hawthorn, F. Ronning, R. W. Hill, M. Sutherland, L. Taillefer, and C. Petrovic, Phys. Rev. Lett. **97**, 106606 (2006).
[20] M. Yokoyama, K. Suzuki, K. Tenya, S. Nakamura, Y. Kono, S. Kittaka, and T. Sakakibara, Phys. Rev. B **99**, 054506 (2019).
[21] J. Paglione, M. A. Tanatar, J.-P. Reid, H. Shakeripour, C. Petrovic, and L. Taillefer, Phys. Rev. Lett. **117**, 016601 (2016).
[22] Y. P. Liu, Y. J. Zhang, J. J. Dong, H. Lee, Z. X. Wei, W. L. Zhang, C. Y. Chen, H. Q. Yuan, Y.-f. Yang, and J. Qi, Phys. Rev. Lett. **124**, 057404 (2020).
[23] N. P. Armitage, E. J. Mele, and A. Vishwanath, Rev. Mod. Phys. **90**, 015001 (2018).
[24] S. Dzsaber, L. Prochaska, A. Sidorenko, G. Eguchi, R. Svagera, M. Waas, A. Prokofiev, Q. Si, and S. Paschen, Phys. Rev. Lett. **118**, 246601 (2017).
[25] S. E. Grefe, H.-H. Lai, S. Paschen, and Q. Si, Phys. Rev. B **101**, 075138 (2020).
[26] C. Cao, G.-X. Zhi, and J.-X. Zhu, Phys. Rev. Lett. **124**, 166403 (2020).
[27] J. Schweizer, F. Givord, J.-X. Boucherle, F. Bourdarot, and E. Ressouche, J. Phys.: Condens. Matter **20**, 135204 (2008).
[28] K. Andres, J. E. Graebner, and H. R. Ott, Phys. Rev. Lett. **35**, 1779 (1975).
[29] H. Nakamura, Y. Kitaoka, K. Asayama, and J. Flouquet, J. Phys. Soc. Jpn. **57**, 2644 (1988).
[30] M. Sera, T. Satoh, and T. Kasuya, J. Magn. Magn. Mater. **63–64**, 82 (1987).
[31] Y.-Y. Chen, J. M. Lawrence, J. D. Thompson, and J. O. Willis, Phys. Rev. B **40**, 10766 (1989).
[32] Y. Y. Chen, Y. D. Yao, B. C. Hu, C. H. Jang, J. M. Lawrence, H. Huang, and W. H. Li, Phys. Rev. B **55**, 5937 (1997).
[33] W.-H. Li, J. C. Peng, Y.-C. Lin, K. C. Lee, J. W. Lynn, and Y. Y. Chen, J. Appl. Phys. **83**, 6426 (1998).
[34] D. Singh, S. Yadam, D. Venkateshwarlu, M. Gangrade, S. S. Samatham, and V. Ganesan, Mater. Res. Express **1**, 046114 (2014).
[35] P. Nozières, Eur. Phys. J. B **6**, 447 (1998).

[36] S. Sachdev, Phys. Rev. B **45**, 12377 (1992).
[37] G. Kotliar, S. Y. Savrasov, K. Haule, V. S. Oudovenko, O. Parcollet, and C. A. Marianetti, Rev. Mod. Phys. **78**, 865 (2006).
[38] A. Georges, G. Kotliar, W. Krauth, and M. J. Rozenberg, Rev. Mod. Phys. **68**, 13 (1996).
[39] E. A. Goremychkin, H. Park, R. Osborn, S. Rosenkranz, J.-P. Castellan, V. R. Fanelli, A. D. Christianson, M. B. Stone, E. D. Bauer, K. J. McClellan, D. D. Byler, and J. M. Lawrence, Science **359**, 186 (2018).
[40] J. H. Shim, K. Haule, and G. Kotliar, Science **318**, 1615 (2007).
[41] L. Huang and H. Lu, Phys. Rev. B **99**, 045122 (2019).
[42] H. Lu and L. Huang, Phys. Rev. B **98**, 195102 (2018).
[43] K. Haule, C.-H. Yee, and K. Kim, Phys. Rev. B **81**, 195107 (2010).
[44] H. Lu and L. Huang, Phys. Rev. B **94**, 075132 (2016).
[45] P. Blaha, K. Schwarz, G. Madsen, D. Kvasnicka, and J. Luitz, *WIEN2k, an Augmented Plane Wave + Local Orbitals Program for Calculating Crystal Properties* (Karlheinz Schwarz, Technische Universität Wien, Vienna, 2001).
[46] J. P. Perdew, K. Burke, and M. Ernzerhof, Phys. Rev. Lett. **77**, 3865 (1996).
[47] K. Haule, Phys. Rev. Lett. **115**, 196403 (2015).
[48] K. Haule, Phys. Rev. B **75**, 155113 (2007).
[49] P. Werner, A. Comanac, L. de' Medici, M. Troyer, and A. J. Millis, Phys. Rev. Lett. **97**, 076405 (2006).
[50] E. Gull, A. J. Millis, A. I. Lichtenstein, A. N. Rubtsov, M. Troyer, and P. Werner, Rev. Mod. Phys. **83**, 349 (2011).
[51] H. Lu and L. Huang, Phys. Rev. B **95**, 155140 (2017).
[52] K. Haule, S. Kirchner, J. Kroha, and P. Wölfle, Phys. Rev. B **64**, 155111 (2001).
[53] P. Zhang, B. Liu, S. Zhang, K. Haule, and J. Dai, arXiv:1909.13251.
[54] J.-X. Zhu, R. C. Albers, K. Haule, and J. M. Wills, Phys. Rev. B **91**, 165126 (2015).
[55] Y. Luo, F. Ronning, N. Wakeham, X. Lu, T. Park, Z.-A. Xu, and J. D. Thompson, Proc. Natl. Acad. Sci. USA **112**, 13520 (2015).
[56] M. Jarrell and J. Gubernatis, Phys. Rep. **269**, 133 (1996).
[57] Z. Lin, J.-H. Choi, Q. Zhang, W. Qin, S. Yi, P. Wang, L. Li, Y. Wang, H. Zhang, Z. Sun, L. Wei, S. Zhang, T. Guo, Q. Lu, J.-H. Cho, C. Zeng, and Z. Zhang, Phys. Rev. Lett. **121**, 096401 (2018).
[58] L. Ye, M. K. Chan, R. D. McDonald, D. Graf, M. Kang, J. Liu, T. Suzuki, R. Comin, L. Fu, and J. G. Checkelsky, Nat. Commun. **10**, 4870 (2019).
[59] J.-X. Yin, S. S. Zhang, H. Li, K. Jiang, G. Chang, B. Zhang, B. Lian, C. Xiang, I. Belopolski, H. Zheng, T. A. Cochran, S.-Y. Xu, G. Bian, K. Liu, T.-R. Chang, H. Lin, Z.-Y. Lu, Z. Wang, S. Jia, W. Wang, and M. Z. Hasan, Nature (London) **562**, 91 (2018).
[60] L. Ye, M. Kang, J. Liu, F. von Cube, C. R. Wicker, T. Suzuki, C. Jozwiak, A. Bostwick, E. Rotenberg, D. C. Bell, L. Fu, R. Comin, and J. G. Checkelsky, Nature (London) **555**, 638 (2018).
[61] Q. Wang, Q. Yin, and H. Lei, Chin. Phys. B **29**, 017101 (2020).
[62] K. Kim, J. Seo, E. Lee, K. T. Ko, B. S. Kim, B. G. Jang, J. M. Ok, J. Lee, Y. J. Jo, W. Kang, J. H. Shim, C. Kim, H. W. Yeom, B. I. Min, B.-J. Yang, and J. S. Kim, Nat. Mater. **17**, 794 (2018).
[63] E. Liu, Y. Sun, N. Kumar, L. Muechler, A. Sun, L. Jiao, S.-Y. Yang, D. Liu, A. Liang, Q. Xu, J. Kroder, V. Süß, H. Borrmann, C. Shekhar, Z. Wang, C. Xi, W. Wang, W. Schnelle, S. Wirth, Y. Chen, S. T. B. Goennenwein, and C. Felser, Nat. Phys. **14**, 1125 (2018).
[64] Q. Wang, Y. Xu, R. Lou, Z. Liu, M. Li, Y. Huang, D. Shen, H. Weng, S. Wang, and H. Lei, Nat. Commun. **9**, 3681 (2018).
[65] J.-X. Yin, S. S. Zhang, G. Chang, Q. Wang, S. S. Tsirkin, Z. Guguchia, B. Lian, H. Zhou, K. Jiang, I. Belopolski, N. Shumiya, D. Multer, M. Litskevich, T. A. Cochran, H. Lin, Z. Wang, T. Neupert, S. Jia, H. Lei, and M. Z. Hasan, Nat. Phys. **15**, 443 (2019).
[66] R. Yang, T. Zhang, L. Zhou, Y. Dai, Z. Liao, H. Weng, and X. Qiu, Phys. Rev. Lett. **124**, 077403 (2020).
[67] Z. Lin, C. Wang, P. Wang, S. Yi, L. Li, Q. Zhang, Y. Wang, Z. Wang, H. Huang, Y. Sun, Y. Huang, D. Shen, D. Feng, Z. Sun, J.-H. Cho, C. Zeng, and Z. Zhang, Phys. Rev. B **102**, 155103 (2020).
[68] M. Kang, L. Ye, S. Fang, J.-S. You, A. Levitan, M. Han, J. I. Facio, C. Jozwiak, A. Bostwick, E. Rotenberg, M. K. Chan, R. D. McDonald, D. Graf, K. Kaznatcheev, E. Vescovo, D. C. Bell, E. Kaxiras, J. van den Brink, M. Richter, M. Prasad Ghimire, J. G. Checkelsky, and R. Comin, Nat. Mater. **19**, 163 (2020).
[69] Z. Liu, M. Li, Q. Wang, G. Wang, C. Wen, K. Jiang, X. Lu, S. Yan, Y. Huang, D. Shen, J.-X. Yin, Z. Wang, Z. Yin, H. Lei, and S. Wang, Nat. Commun. **11**, 4002 (2020).
[70] M. Kang, S. Fang, L. Ye, H. C. Po, J. Denlinger, C. Jozwiak, A. Bostwick, E. Rotenberg, E. Kaxiras, J. G. Checkelsky, and R. Comin, Nat. Commun. **11**, 4004 (2020).
[71] Y. Zhang, H. Lu, X. Zhu, S. Tan, W. Feng, Q. Liu, W. Zhang, Q. Chen, Y. Liu, X. Luo, D. Xie, L. Luo, Z. Zhang, and X. Lai, Sci. Adv. **4**, eaao6791 (2018).